

# Apparent Diffusion Coefficients from High Angular Resolution Diffusion Imaging: Estimation and Applications

Maxime Descoteaux,<sup>1\*</sup> Elaine Angelino,<sup>2</sup> Shaun Fitzgibbons,<sup>2</sup> and Rachid Deriche<sup>1</sup>

**High angular resolution diffusion imaging has recently been of great interest in characterizing non-Gaussian diffusion processes. One important goal is to obtain more accurate fits of the apparent diffusion processes in these non-Gaussian regions, thus overcoming the limitations of classical diffusion tensor imaging. This paper presents an extensive study of high-order models for apparent diffusion coefficient estimation and illustrates some of their applications. Using a meaningful modified spherical harmonics basis to capture the physical constraints of the problem, a new regularization algorithm is proposed. The new smoothing term is based on the Laplace-Beltrami operator and its closed form implementation is used in the fitting procedure. Next, the linear transformation between the coefficients of a spherical harmonic series of order  $\ell$  and independent elements of a rank- $\ell$  high-order diffusion tensor is explicitly derived. This relation allows comparison of the state-of-the-art anisotropy measures computed from spherical harmonics and tensor coefficients. Published results are reproduced accurately and it is also possible to recover voxels with isotropic, single fiber anisotropic, and multiple fiber anisotropic diffusion. Validation is performed on apparent diffusion coefficients from synthetic data, from a biological phantom, and from a human brain dataset. Magn Reson Med 56:395–410, 2006. © 2006 Wiley-Liss, Inc.**

**Key words:** high angular resolution diffusion imaging; spherical harmonics; Laplace-Beltrami operator; regularization; high-order diffusion tensor; anisotropy measures

For the past decade, there has been growing interest in diffusion magnetic resonance imaging (MRI) to understand functional coupling between cortical regions of the brain, for characterization of neurodegenerative diseases, for surgical planning, and for other medical applications. Diffusion MRI is the only noninvasive tool to obtain information about the neural architecture *in vivo*. It is based on the Brownian motion of water molecules in normal tissues and the observation that molecules tend to diffuse along fibers when contained in fiber bundles (1,2). Using classic diffusion tensor imaging (DTI), several methods have been developed to segment and track white matter fibers in the human brain (3–8). The common way to analyze the data

is to fit it to a second-order tensor, which corresponds to the probability distribution of a given water molecule moving by a certain amount during some fixed elapsed time. By diagonalization, the surface corresponding to the diffusion tensor is an ellipsoid with its long axis aligned with the fiber orientation. However, the theoretical basis for this model assumes that the underlying diffusion process is Gaussian. While this approximation is adequate for voxels in which there is only a single fiber orientation (or none), it breaks down for voxels in which there is more complicated internal structure, as seen in Fig. 1, an example of two fibers crossing. This is an important limitation, since the resolution of DTI acquisition is between 1 and 3 mm<sup>3</sup>, while the physical diameter of fibers can be less than 1  $\mu$ m and up to 30  $\mu$ m (9). From anisotropy measure maps, we know that many voxels in diffusion MRI volumes potentially have multiple fibers with crossing, kissing, or diverging configurations.

To date, this is a reason why clinicians and neurosurgeons have been skeptical of tracking and segmentation methods developed on DTI data. They have doubts on the principal directions extracted and followed from the diffusion tensor to track fiber bundles. In the presence of multiple fibers, the diffusion profile is oblate or planar and there is no unique principal direction (Fig. 1). Additionally, note that the maxima of the apparent diffusion coefficient (ADC) profile do not correspond to true fiber orientation (thin green lines). In current clinical applications, people instead choose to use simple anisotropy maps computed from the ADC profile (10) to infer white matter connectivity information. These measures are fast and easy to interpret with regions of anisotropy that clearly stand out. Many anisotropy measures exist and the most commonly used are fractional anisotropy (FA) and relative anisotropy (RA) (11), but again, these measures are limited in non-Gaussian diffusion areas when computed from DTI data. This is well illustrated by Ozarslan et al. (12) where the anisotropy measure in a fiber crossing region is in the same range as voxels with no structure. As such, recent research has been done to generalize the existing diffusion model with new higher resolution acquisition techniques such as high angular resolution diffusion imaging (HARDI) (13). One natural generalization is to model the apparent diffusion coefficient with higher-order diffusion tensors (HODT) (14). This model does not assume any a priori knowledge about the diffusivity profile and has the potential to describe non-Gaussian diffusion.

In this article, we study the estimation of the ADC profile from HARDI data and its ability to describe complex tissue architecture. Contrary to most recent papers on HARDI data processing, we do not focus on finding the

<sup>1</sup>Odyssee Project Team, INRIA Sophia-Antipolis/ENPC-Paris/ENS-Ulm Paris, France

<sup>2</sup>Harvard University, Boston, Massachusetts

Grant sponsor: FFCR; Grant Sponsor: CRSNG Canada graduate scholarship; Grant sponsor: INRIA International Internships; Grant sponsor: NSF-INRIA Cooperative Research.

Correspondence to: Maxime Descoteaux, INRIA, Odyssee Project Team, 2004 route des Lucioles, 06902 Sophia Antipolis, France. E-mail: Maxime.Descoteaux@sophia.inria.fr

Received 21 September 2005; revised 30 March 2006; accepted 6 April 2006  
DOI 10.1002/mrm.20948

Published online 26 June 2006 in Wiley InterScience (www.interscience.wiley.com).

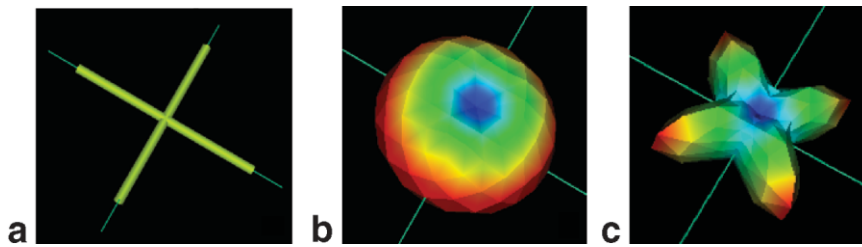


Fig. 1. ADC profile estimate for a 2-fiber distribution (a). Diffusion tensor profile (b) fails to recover multiple fiber orientation whereas the HARDI ADC profile (c) has multiple peaks. Note that the maxima of the ADC profile do not agree with thin green lines corresponding to the true synthetic fiber directions. [Color figure can be viewed in the online issue, which is available at [www.interscience.wiley.com](http://www.interscience.wiley.com).]

orientation of underlying fibers but want to design the appropriate tools to describe noisy HARDI data and explore scalar anisotropy measures computed from high-order formulation. In particular, the paper addresses the problem of fitting HARDI data with a higher-order tensor. One proposed possibility by Ozarslan et al. (14) is to use a direct linear regression by least-squares fitting. This can be effective but its robustness to noise is questionable as there does not appear to be any straightforward way to impose viable smoothness maximizing (regularization) criteria. We approach the problem with a spherical harmonics series approximation (15–17). An important contribution of our work is to propose a generalization of the standard least-squares evaluation method to include a regularization criterion. From this result, we compute the linear transformation taking the coefficients of the spherical harmonic series to the independent elements of the HODT using the relation presented in (14). Therefore, any technique developed for spherical harmonic formulation can be quickly and easily applied to the high-order diffusion tensor formulation and vice versa. This bridge is very useful for comparison purposes between state-of-the-art anisotropy measures for high-order models computed from spherical harmonics and tensor coefficients. Published results are reproduced accurately and it is also possible to recover voxels with isotropic, single fiber anisotropic, and multiple fiber anisotropic diffusion.

## THEORY

### High Angular Resolution Diffusion Imaging

Diffusion MRI, introduced in the mid 1980s by Le Bihan et al. (1), has become intensely used for the past 10 years due to important image acquisition improvement. It is the unique noninvasive technique capable of quantifying the anisotropic diffusion of water in biological tissues such as

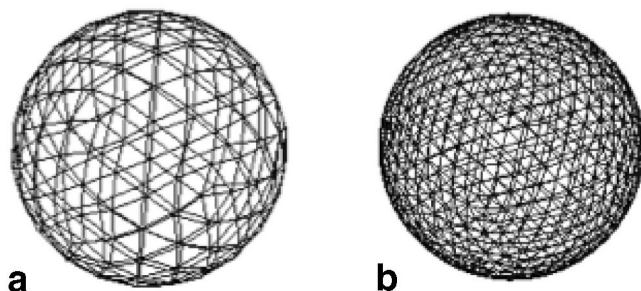


Fig. 2. Discrete sampling of the sphere for 162 (a) and 252 (b) gradient directions corresponding to order 3 and order 4 tessellation of the icosahedron, respectively.

muscle and brain white matter. Shortly after the first acquisition of images characterizing the anisotropic diffusion of water molecules, Bassler et al. proposed the diffusion tensor model (2). DTI computes the ADC based on the assumption that the diffusion or Brownian motion of water molecules can be described by a zero-mean Gaussian distribution. The diffusion process is then fully described by a rank-2 diffusion tensor  $\mathbf{D}$ , which is a positive-definite  $3 \times 3$  symmetric matrix. Using a minimum of six different encoded unit gradient directions  $\mathbf{g}$ , the diffusion tensor can be constructed at each voxel in the volume. The resulting signal attenuation is given by the Stejskal–Tanner (18) equation.  $S(\mathbf{g}) = S_0 \exp(-b\mathbf{g}^T\mathbf{D}\mathbf{g})$ , where  $b$  is the diffusion weighting factor depending on scanner parameters such as the length and strength of the diffusion gradient and time between diffusion gradient pulses,  $S_0$  is the  $T_2$ -weighted signal acquired without any diffusion gradients, and  $D(\mathbf{g}) = \mathbf{g}^T\mathbf{D}\mathbf{g}$  is the ADC along gradient direction  $\mathbf{g} = \mathbf{g}(\theta, \phi) = (\sin \theta \cos \phi, \sin \theta \sin \phi, \cos \theta)^T$ , where  $(\theta, \phi)$  obey physics convention ( $\theta \in [0, \pi]$ ,  $\phi \in [0, 2\pi]$ ). Numerous methods for estimating and regularizing the diffusion tensor have been proposed (3–5,19). Segmentation and tractography on known fiber bundles with clear anisotropic regions of single fiber bundles work well (6,8) but the approaches are intrinsically limited and unstable in regions of multiple fibers due to the restrictive assumption of the diffusion tensor model.

In order to better describe the complexity of water motion, a clinically feasible approach, HARDI, has been proposed by Tuch et al. (20). At the cost of longer acquisition times, the idea is to sample the sphere in discrete gradient directions (Fig. 2) and compute the ADC profile  $D(\mathbf{g})$  along each gradient direction  $\mathbf{g}(\theta, \phi)$ .

Hence, at each voxel, we have a discrete spherical function with no a priori assumption about the nature of the diffusion process within the voxel. There have been interesting works done recently on alternative ways to obtain complex subvoxel tissue architecture, such as diffusion spectrum imaging (21),  $q$ -ball imaging (22), and persistent angular structure MRI (23). These reconstruction methods aim to recover the orientations of the underlying fiber distribution by estimating the probability density function the orientation distribution function, and the persistent angular structure of the water molecules, respectively.<sup>1</sup> However, in this paper, we focus on HARDI data and, in particular, the development of new and efficient techniques to process noisy spherical data acquired in multi-

<sup>1</sup>A detailed discussion on these high angular resolution reconstruction methods can be found in (24).

ple directions. Several recent approaches have attempted to estimate and investigate properties of noisy spherical data obtained from HARDI (14–17,20) to characterize tissues with non-Gaussian diffusion. The problem is to recover a smooth ADC,  $D(\mathbf{g})$ , close to the true ADC from the measured diffusion MRI noisy signal  $S(\mathbf{g})$ , where

$$D(\mathbf{g}) = -\frac{1}{b} \ln\left(\frac{S(\mathbf{g})}{S_0}\right). \quad [1]$$

There are two classes of algorithms for ADC profile estimation. The first uses a truncated spherical harmonic series to approximate the function on the sphere (15–17), whereas the other fits a high-order diffusion tensor to the data (14). Before discussing the fitting of data to a spherical harmonic series, we first define the spherical harmonics and discuss briefly some of their important properties.

### Spherical Harmonics

The spherical harmonics (SH), normally indicated by  $Y_\ell^m$  ( $\ell$  denotes the order and  $m$  the phase factor), are a basis for complex functions on the unit sphere satisfying the SH differential equation

$$\frac{1}{\sin\theta} \frac{\partial}{\partial\theta} \left( \sin\theta \frac{\partial F}{\partial\theta} \right) + \frac{1}{\sin^2\theta} \frac{\partial^2 F}{\partial\phi^2} + \ell(\ell + 1)F = 0, \quad \ell \in \mathbb{Z}_+. \quad [2]$$

The first two terms of this equation correspond to the Laplacian in spherical coordinates, also called the three dimensional Laplace–Beltrami operator  $\Delta_b$ . It is a natural measure of smoothness for functions defined on the unit sphere and has been used in many image processing applications (26,27). Furthermore, it is particularly easy to work with for applications involving the spherical harmonics because, referring to Eq. [2], the spherical harmonics satisfy the relation  $\Delta_b Y_\ell^m = -\ell(\ell + 1)Y_\ell^m$ .

For each nonnegative integer  $\ell$  there are exactly  $2\ell + 1$  spherical harmonics given by  $Y_\ell^{-\ell}, \dots, Y_\ell^0, \dots, Y_\ell^\ell$ , i.e.,  $m = -\ell, \dots, 0, \dots, \ell$ . Explicitly, they are given as

$$Y_\ell^m(\theta, \phi) = \sqrt{\frac{2\ell + 1}{4\pi} \frac{(\ell - m)!}{(\ell + m)!}} P_\ell^m(\cos\theta) \exp(im\phi), \quad [3]$$

where  $P_\ell^m$  is an associated Legendre polynomial. The normalization factor in Eq. [3] is chosen so that the spherical harmonics form an orthonormal set of functions with respect to the inner product  $\langle f, g \rangle = \int_\Omega f^* g d\Omega$ , where integration over  $\Omega$  denotes integration over the unit sphere and  $f^*$  denotes the complex conjugate of  $f$ . Finally, it is easy to show that even order spherical harmonics are antipodally symmetric while the odd order spherical harmonics are antipodally antisymmetric (28). We will be using these important properties in the development of our regularization algorithm.

### Methods for Fitting Spherical Data with SH Series

The set of spherical harmonics forms an orthonormal basis for all functions on the unit sphere. High-order spherical

harmonics correspond to high frequency modes of the unit sphere, and thus a truncated spherical harmonic series can be effectively used to fit relatively smooth functions. Since they form a basis, any spherical function  $x: S^2 \rightarrow C$  can be written as  $x(\theta, \phi) = \sum_{\ell=0}^\infty \sum_{m=-\ell}^\ell c_\ell^m Y_\ell^m(\theta, \phi)$ . Moreover, due to orthonormality of the SH basis, the coefficients of the SH series  $c_\ell^m$  can be calculated by forming the inner product of  $x$  with the spherical harmonics,  $c_\ell^m = \langle x(\theta, \phi), Y_\ell^m(\theta, \phi) \rangle = \int_0^{2\pi} \int_0^\pi x(\theta, \phi) Y_\ell^m(\theta, \phi) \sin\theta d\theta d\phi$ . This idea was first used to fit the ADC profile obtained from HARDI data by Frank in (15) where the function  $x$  is replaced by the discrete sampling of the diffusivities,  $D(\mathbf{g})$ . Frank performs the direct discretization of the integrals. This is a computationally poor method to obtain the coefficients and recent salient work by Alexander et al. (16) use a linear least-squares method to solve for the unknowns. This linear least-squares method was first proposed in the vision community for the parameterization of closed surfaces for 3D shape description by Brechbuhler et al. (29). Letting  $n_s$  be the number of discrete points on the sphere,  $N$  the number of SH used in the approximation of order  $\ell$  ( $n_s \gg N$ ),  $\mathbf{X} = (x_1, \dots, x_{n_s})^T$  the vector of ADCs  $D(\mathbf{g})$ ,  $\mathbf{C} = (c_0^0, c_1^{-1}, c_1^0, \dots, c_\ell^\ell)^T$  the vector of SH coefficients, and

$$\mathbf{B} = \begin{pmatrix} Y_0^0(\theta_1, \phi_1) & Y_1^{-1}(\theta_1, \phi_1) & \dots & Y_\ell^\ell(\theta_1, \phi_1) \\ \vdots & \vdots & \ddots & \vdots \\ Y_0^0(\theta_{n_s}, \phi_{n_s}) & Y_1^{-1}(\theta_{n_s}, \phi_{n_s}) & \dots & Y_\ell^\ell(\theta_{n_s}, \phi_{n_s}) \end{pmatrix} \quad [4]$$

the  $n_s \times N$  matrix of discrete SH, the approach seeks for the spherical harmonic series that passes nearest to the discrete samplings on the sphere. Hence,  $\mathbf{X} = \mathbf{B}\mathbf{C} + \mathbf{E}$  where the error vector  $\mathbf{E}$  should be small. This system of overdetermined equations is solved with linear least-square sums over the columns of  $\mathbf{E}$  by minimizing  $\|\mathbf{X} - \mathbf{B}\mathbf{C}\|^2$ , yielding

$$\mathbf{C} = (\mathbf{B}^T \mathbf{B})^{-1} \mathbf{B}^T \mathbf{X}. \quad [5]$$

Note that this is an unweighted linear least-squares fit and that it can be simply extended to a weighted fit, as in (2), to account for the expected variation in each diffusion coefficient and distortions introduced by the logarithmic transformation of Eq. [1]. The vector  $\mathbf{C}$  of spherical harmonic coefficients gives the best-fitting truncated series to the ADC profile. The estimated ADC profile of order  $\ell$  is thus recovered by evaluating  $D(\mathbf{g}(\theta, \phi)) = \sum_{k=0}^\ell \sum_{m=-k}^k c_k^m Y_k^m(\theta, \phi)$  for any  $(\theta, \phi)$  outside the discrete measurements  $\mathbf{X}$  or in the discrete linear case, by simple matrix multiplication,

$$\mathbf{X} = \mathbf{B}\mathbf{C}. \quad [6]$$

Though this works fairly well so long as noise is kept small, we propose, in this paper, a more general fitting procedure that takes advantage of the properties of spherical harmonics and the Laplace–Beltrami operator to quantify the smoothness of spherical functions. Before doing so, we review the relationship between the spherical harmonic series of order- $\ell$  and the higher order diffusion tensor of rank- $\ell$ .

### Fitting the ADC Profile with a High-Order Diffusion Tensor

In (14), instead of fitting the ADC profile with a rank-2 tensor, the diffusivities are expressed in terms of a HODT. Replacing the classical rank-2 tensor  $\mathbf{D}$  by a HODT into the standard Stejskal–Tanner leads to a generalized Stejskal–Tanner equation (14, Eq. [11]). This model assumes no a priori knowledge of the diffusion profile. However, one must assume that a rank- $\ell$  tensor is sufficient to determine the ADC profile,  $\mathbf{X}$ . Given this assumption, it is possible to simplify the problem by noting that the diffusion tensor must be totally symmetric, which means that the HODT can be fully expressed in terms of its independent elements, whose vector representation is denoted by  $\mathbf{T}$  for the rest of the paper. Hence, the authors of (14) rewrite the expression for each ADC  $D(\mathbf{g}(\theta_i, \phi_i))$  along direction  $\mathbf{g}(\theta_i, \phi_i)$  in a more compact form,

$$D(\mathbf{g}(\theta_i, \phi_i)) = \sum_{k=1}^N \mu_k T_k \prod_{p=1}^{\ell} g_{k(p)}(\theta_i, \phi_i), \quad [7]$$

where  $N$  is the number of independent elements of  $\mathbf{T}$ ,  $T_k$  is the  $k$ th independent element of the HODT vector representation  $\mathbf{T}$ ,  $\mu_k$  is the corresponding multiplicity of the element, and  $g_{k(p)}$  gives the component of the gradient direction corresponding to the  $p$ th index of the  $k$ th independent element of the tensor. The complete derivation is in (14) and an explicit example is shown in (28).

Ozarslan et al. (12,14) fit the ADC profile with a HODT (Eq. [7]) using linear regression with processing routines written in IDL (Research Systems, Inc., Boulder, CO, USA). We are not sure of the exact routines used in this procedure but we have implemented a standard linear regression with least-squares fitting as described in the previous section. Letting  $\mathbf{X}$  represent the ADC profile,  $\mathbf{T}$  the vector representation of the HODT independent elements, and  $\mathbf{R}$  the  $n_s \times N$  matrix

$$\mathbf{R} = \begin{pmatrix} \mu_1 \prod_{p=1}^{\ell} g_{1(p)}(\theta_1, \phi_1) & \cdots & \mu_N \prod_{p=1}^{\ell} g_{N(p)}(\theta_1, \phi_1) \\ \vdots & \ddots & \vdots \\ \mu_1 \prod_{p=1}^{\ell} g_{1(p)}(\theta_{n_s}, \phi_{n_s}) & \cdots & \mu_N \prod_{p=1}^{\ell} g_{N(p)}(\theta_{n_s}, \phi_{n_s}) \end{pmatrix}, \quad [8]$$

we define an error term  $\mathbf{E}'$  so that  $\mathbf{X} = \mathbf{R}\mathbf{T} + \mathbf{E}'$ . We seek to minimize the quantity  $\mathbf{E}'^T \mathbf{E}'$  using the same techniques described previously. We then obtain the expansion for the HODT,

$$\mathbf{T} = (\mathbf{R}^T \mathbf{R})^{-1} \mathbf{R}^T \mathbf{X}. \quad [9]$$

The estimated ADC profile is thus recovered by evaluating Eq. [7] for any  $(\theta, \phi)$  outside the discrete measurements or in the discrete case, by simple matrix multiplication,

$$\mathbf{X} = \mathbf{R}\mathbf{T}. \quad [10]$$

The method does not have a smoothing or regularization parameter and will therefore be more sensitive to noise.

### A Regularization Algorithm for ADC Profile Estimation

The first step in our method is to take raw HARDI ADC profile data and fit it to a truncated spherical harmonic series. There are five primary constraints on the diffusivity profile that must be considered in the optimization of this fit. It must be (1) real, (2) antipodally symmetric, (3) positive, (4) relatively smooth, and (5) in close agreement with the measured data. Constraints (1), (2), and (3) are physical constraints due to the nature of diffusion MRI acquisition. We deal with the first two straightforwardly by a special choice of modified spherical harmonic basis. In order to impose the antipodal symmetry constraint on the expansion, we consider only spherical harmonics of even degree. As mentioned before, spherical harmonics of odd order are antipodally anti-symmetric, while spherical harmonics of even order are antipodally symmetric. In order to impose the real-valued constraint, we consider a basis of real linear combinations of the spherical harmonics as the basis. In this modified basis, the real-valued constraint on the ADC profile can be taken into consideration simply by optimizing the fit over the set of real coefficients. The idea of modeling the ADC profile with physical constraints was proposed by Chen et al. (17) where they also use only even order SHs and construct a constrained minimization problem forcing the ADC profile estimate to be real and positive. Our approach is slightly different in that we make sure that we add a smoothing term as discussed later and also enforce the real-valued constraint simply by our choice of a modified spherical harmonic basis, rather than by implementing a complicated constrained minimization routine.

For a given order  $\ell$ , we let  $k = 0, 2, 4, \dots, \ell$  and  $m = -k, \dots, 0, \dots, k$ , we define new index  $j := j(k, m) = (k^2 + k + 2)/2 + m$  and define our modified basis  $\mathbf{Y}$  with  $N = (1/2)(\ell + 1)(\ell + 2)$  elements  $Y_j$  such that

$$Y_j = \begin{cases} \sqrt{2} \cdot \text{Re}(Y_k^m), & \text{if } -k \leq m < 0 \\ Y_k^0 & \text{if } m = 0 \\ \sqrt{2} \cdot \text{Im}(Y_k^m), & \text{if } 0 < m \leq k \end{cases}, \quad [11]$$

where  $\text{Re}(Y_\ell^m)$  and  $\text{Im}(Y_\ell^m)$  represent the real and imaginary parts of  $Y_\ell^m$  respectively.

A detailed expansion of the rank-4 modified basis is given in (28) and the rank-2 basis is given in Fig. 3. Note that the constants in front of the composed terms ensure orthonormality with respect to the inner product defined earlier. For the rest of the paper,  $\mathbf{Y} = (Y_1, \dots, Y_N)^T$  will refer to the modified spherical harmonic basis. Now, we can reformulate the approximation of the diffusivity profile at each discrete sampling  $\mathbf{g}(\theta_i, \phi_i)$  as

$$D(\mathbf{g}(\theta_i, \phi_i)) = \sum_{j=1}^N c_j Y_j(\theta_i, \phi_i) \quad [12]$$

to determine the coefficients  $c_j$ . As before, we use noisy HARDI data sampled at a set of  $n_s$  points  $(\theta_i, \phi_i)$  on the

sphere and we can write the equations given above as an overdetermined unweighted linear system  $\mathbf{X} = \mathbf{B}\mathbf{C} + \mathbf{E}$ , but now with matrix  $\mathbf{B}$  constructed with the modified spherical harmonics basis. At this point, instead of performing a simple least-squares minimization from which we obtain the result given in Eq. [5], we want to add a regularization to our fitting procedure. We propose to find the solution that minimizes the sum of the previously discussed squared error term and the new smoothness term. We define a measure of the deviation from smoothness  $E$  of a function  $f$  defined on the unit sphere as  $E(f) = \int_{\Omega} (\Delta_b f)^2 d\Omega$ , where integration over  $\Omega$  denotes, as before, integration over the unit sphere and  $\Delta_b$  is the Laplace–Beltrami operator. The Laplace–Beltrami operator is a natural measure of smoothness for functions defined on the unit sphere and we know that the spherical harmonics satisfy the relation  $\Delta_b Y_\ell^m = -\ell(\ell + 1)Y_\ell^m$ . Note that this relation also holds for our modified SH basis. Using the orthonormality property of the modified basis, the above functional can be rewritten straightforwardly in terms of the coefficient vector  $\mathbf{C}$  as follows:

$$E(f) = \int_{\Omega} \Delta_b \left( \sum_p c_p Y_p \right) \Delta_b \left( \sum_q c_q Y_q \right) d\Omega = \sum_{j=1}^N c_j^2 \ell_j^2 (\ell_j + 1)^2 = \mathbf{C}^T \mathbf{L} \mathbf{C}, \quad [13]$$

where  $\mathbf{L}$  is simply the  $N \times N$  matrix with entries  $\ell_j^2 (\ell_j + 1)^2$  along the diagonal,  $L_{jj}$ . Therefore, the quantity we wish to minimize can be expressed in matrix form as

$$M(\mathbf{C}) = (\mathbf{X} - \mathbf{B}\mathbf{C})^T (\mathbf{X} - \mathbf{B}\mathbf{C}) + \lambda \mathbf{C}^T \mathbf{L} \mathbf{C} \quad [14]$$

where  $\lambda$  is a variable weighting factor on the regularization term. The coefficient vector minimizing this expression can then be determined just as in the standard unweighted linear least-squares fit ( $\lambda = 0$ ), by setting each of the  $\partial M / \partial c_j = 0$ , from which we obtain the generalized expression for the desired spherical harmonic series coefficient vector

$$\mathbf{C} = (\mathbf{B}^T \mathbf{B} + \lambda \mathbf{L})^{-1} \mathbf{B}^T \mathbf{X}. \quad [15]$$

The estimated ADC profile is thus recovered by evaluating  $D(\mathbf{g}(\theta, \phi)) = \sum_{j=1}^N c_j Y_j(\theta, \phi)$  for any  $(\theta, \phi)$  outside the discrete measurements or in the discrete case, matrix multiplication Eq. [6] as before. Note that a variation on the above derivation will hold in other geometries if a proper basis of functions is chosen. Intuitively, this approach penalizes an approximation function for having higher-order terms in its modified SH series. Therefore, higher-order terms will only be included in the fit if they significantly improve the overall accuracy of the approximation. This eliminates most of the high-order terms due to noise while leaving those that are necessary to describe the underlying function.

#### From SH Coefficients to HODT Coefficients

We now explicitly derive the correspondence between coefficients of the modified spherical harmonic series and the independent elements of the high-order diffusion tensor.

Ozarslan et al. (14) showed the analytical relationship between the SH coefficients and the independent elements of the HODT. Conceptually, they showed that evaluating the ADC in terms of a rank- $\ell$  HODT is equivalent to fitting the ADC with a spherical harmonics series truncated at order  $\ell$ . In fact, in (28), we proved that both even order spherical harmonics up to order  $\ell$  and rank- $\ell$  HODT polynomials restricted to the sphere are bases for the same function space. Therefore, it is possible to define a general linear transformation  $\mathbf{M}$  between both spaces. We express the coefficients of the modified SH series  $c_j$  in terms of the independent elements of the high-order tensor  $\mathbf{T}$ . From Eq. [12], we have the relation  $c_j = \int_{\Omega} D(\mathbf{g}(\theta, \phi)) Y_j(\theta, \phi)$ . Again assuming that a rank- $\ell$  tensor can describe the diffusion process, we can replace  $D(\mathbf{g})$  with the high-order tensor formulation of Eq. [7] and obtain an expression in matrix form, where  $c_j$  is the  $j$ th element of vector  $\mathbf{C} = \mathbf{M}\mathbf{T}$  and  $N = (1/2)(\ell + 1)(\ell + 2)$  is the number of elements in the SH basis:

$$c_j = \sum_{k=1}^N D_k \int_{\Omega} \mu_k \prod_{p=1}^{\ell} g_{k(p)} Y_j(\theta, \phi) d\Omega \Rightarrow \mathbf{C} = \mathbf{M}\mathbf{T}, \text{ where} \quad [16]$$

$$\mathbf{M} = \begin{pmatrix} \mu_1 \int_{\Omega} \prod_{p=1}^{\ell} g_{1(p)} Y_1(\theta, \phi) d\Omega & \dots & \mu_N \int_{\Omega} \prod_{p=1}^{\ell} g_{N(p)} Y_1(\theta, \phi) d\Omega \\ \vdots & \ddots & \vdots \\ \mu_1 \int_{\Omega} \prod_{p=1}^{\ell} g_{1(p)} Y_N(\theta, \phi) d\Omega & \dots & \mu_N \int_{\Omega} \prod_{p=1}^{\ell} g_{N(p)} Y_N(\theta, \phi) d\Omega \end{pmatrix}. \quad [17]$$

We have also shown in (28, Appendix A) that the  $N \times N$  square matrix  $\mathbf{M}$  is a change-of-basis matrix and thus is invertible. Therefore, given a vector  $\mathbf{C}$  of SH coefficients, we can use  $\mathbf{M}^{-1}$  to compute the corresponding vector of HODT coefficients. We thus obtained a linear mapping between spherical harmonic coefficients and HODT independent elements. Figure 3 illustrates the transformation procedure analytically for the example of the rank-2 diffusion tensor. Note that all matrix entries are *real*, which captures the real-valued constraint on the problem. When using the standard spherical harmonic basis, we obtain (28, Fig. 3) the exact same relationship presented by Ozarslan et al. (14).

Putting everything together, the linear transformation taking the raw HARDI data sampling  $\mathbf{X}$  to the vector  $\mathbf{T}$  of HODT independent coefficients using our regularization method with spherical harmonics is

$$\mathbf{T} = \mathbf{M}^{-1} (\mathbf{B}^T \mathbf{B} + \lambda \mathbf{L})^{-1} \mathbf{B}^T \mathbf{X} \quad [18]$$

The technique is fast because it only involves linear transformations and, more importantly, matrices  $\mathbf{B}$  (Eq. [4]) and  $\mathbf{M}$  (Eq. [17]) are the same for all voxels in the dataset and need only be computed once. Therefore, we have obtained a real and symmetric high-order diffusion tensor and the estimated ADC profile can be recovered, as before, by evaluating Eq. [7] for any  $(\theta, \phi)$  outside the discrete measurements or by simple matrix multiplication in the discrete case (Eq. [10]). In the end, we have a handle on both the SH series coefficients and the independent ele-

$\ell = 2$ , using modified spherical harmonics basis (Eq. [11]):

$$\text{SH basis} := \mathbf{Y} = \begin{pmatrix} 1/(2\sqrt{\pi}) \\ \sqrt{15}/(4\sqrt{\pi}) \sin^2 \theta \cos(2\phi) \\ \sqrt{15}/(2\sqrt{\pi}) \sin \theta \cos \theta \cos \phi \\ \sqrt{5}/(4\sqrt{2\pi})(3 \cos^2 \theta - 1) \\ \sqrt{15}/(2\sqrt{\pi}) \sin \theta \cos \theta \sin \phi \\ \sqrt{15}/(4\sqrt{\pi}) \sin^2 \theta \sin(2\phi) \end{pmatrix}$$

$$\mathbf{M} = \begin{pmatrix} 2\sqrt{\pi}/3 & 0 & 0 & 2\sqrt{\pi}/3 & 0 & 2\sqrt{\pi}/3 \\ 2\sqrt{\pi}/\sqrt{15} & 0 & 0 & -2\sqrt{\pi}/\sqrt{15} & 0 & 0 \\ 0 & 0 & 4\sqrt{\pi}/\sqrt{15} & 0 & 0 & 0 \\ -2\sqrt{\pi}/\sqrt{45} & 0 & 0 & -2\sqrt{\pi}/\sqrt{15} & 0 & 4\sqrt{\pi}/\sqrt{15} \\ 0 & 0 & 0 & 0 & 4\sqrt{\pi}/\sqrt{15} & 0 \\ 0 & 4\sqrt{\pi}/\sqrt{15} & 0 & 0 & 0 & 0 \end{pmatrix}$$

$$\mathbf{T} = \begin{pmatrix} T_{xx} \\ T_{xy} \\ T_{xz} \\ T_{yy} \\ T_{yz} \\ T_{zz} \end{pmatrix} \quad \mathbf{MT} = \mathbf{C} = \begin{pmatrix} 2\sqrt{\pi}/3(T_{xx} + T_{yy} + T_{zz}) \\ 2\sqrt{\pi}/\sqrt{15}(T_{xx} - T_{yy}) \\ 4\sqrt{\pi}/\sqrt{15}T_{xz} \\ -2\sqrt{\pi}/\sqrt{45}(T_{xx} + T_{yy} - 2T_{zz}) \\ 4\sqrt{\pi}/\sqrt{15}T_{yz} \\ 4\sqrt{\pi}/\sqrt{15}T_{xy} \end{pmatrix}$$

ments of the HODT. The important equations of the algorithm and the bridge between SH and HODT coefficients are clearly sketched in Fig. 4.

Finally, note that the physical positive constraint of the ADC profile is not ensured in this derivation. One must make sure that the diffusion tensor is positive definite, i.e.,  $D(\mathbf{g}) > 0$ , for any  $\mathbf{g}$  from Eq. [7]. In implementing our algorithm, we found that this was rarely relevant at reasonable noise levels, as our algorithm gave everywhere positive results without being explicitly constrained to do so. However, in the standard rank-2 DTI problem, methods have been proposed to deal with data where some of the estimated tensors step out of the positive-definite matrix space (7,31,32). In (31), a simple numerical extension of the partial differential equation (PDE) based approach for tensor estimation is proposed to preserve the positive-definite property of each tensor. At each numerical iteration involved with solving the PDE, tensors are diagonalized and reprojected into the space of symmetric semi-positive space by setting the negative eigenvalues to zero.

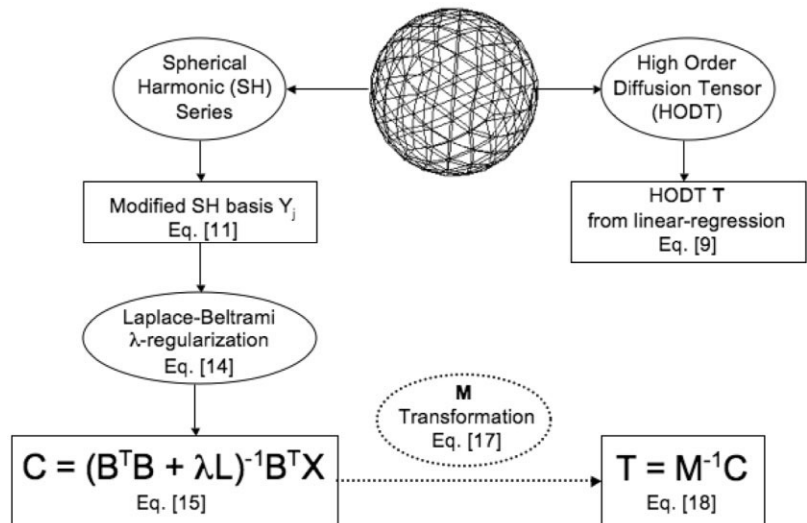
Fig. 3. Rank-2 example of the important matrices in the algorithm. Note that coefficients of  $\mathbf{Y}$  are real. The change-of-basis matrix  $\mathbf{M}$  relating the SH coefficients  $\mathbf{C}$  and HODT independent elements  $\mathbf{T}$  are given.

In (32), the problem is better posed mathematically and PDEs are derived to preserve discontinuities of constrained matrix-valued images. A similar gradient descent approach on the manifold of multivariate normal distributions, which shows promising results, is used in (7) with a Riemannian metric. The question of how to extend this approach in the space of high-order tensors is open and goes beyond the scope of this paper. It is part of the current work to look for numerical schemes in the space of spherical functions parameterized by spherical harmonics that impose  $D(\mathbf{g})$  to be always positive.

#### Finding Optimal Regularization Parameter with the L-Curve Method

As mentioned earlier, the proposed algorithm penalizes the approximated SH and HODT coefficients for having higher-order terms unless they significantly improve the overall accuracy of the estimation. This eliminates most contribution due to noise while leaving those that are

Fig. 4. Sketch of our regularization algorithm. It illustrates the main equations of the method and, most importantly, it shows the bridge between SH coefficients and the independent coefficients of the HODT.



necessary to describe the underlying diffusion profile. However, obtaining this balance depends on choosing a good value for the parameter  $\lambda$ . A popular approach to determine the optimal regularization parameter is the L-curve numerical method (30).

The L-curve is a plot of the norm of a regularized solution versus the norm of the corresponding residual form. The idea is to vary the values of the regularization parameter  $\lambda$  and to plot the points corresponding to regularization errors on the ordinate and the data perturbation errors on the abscissa. In our minimization problem given in equation  $M(\mathbf{C})$  (Eq. [14]), we record the points  $(x,y) = (\|\mathbf{X} - \mathbf{BC}\|^2, \mathbf{C}^T\mathbf{LC})$  while varying  $\lambda$ . This gives a set of noisy points to which one can fit a *best* curve to obtain the L-curve. The optimal  $\lambda$  is then the point on the curve with maximum curvature. This is the location that separates the flatter and more vertical part of the graph, where the solution is dominated by perturbation errors and regularization errors, respectively. In our problem, we choose a 4th-order polynomial least-squares fit, which models the data well.<sup>2</sup> We find parameters  $\{a, b, c, d, e\}$  that best model the data such that  $y(x) = ax^4 + bx^3 + cx^2 + dx + e$ . To find the optimal  $\lambda$ , we seek the discrete point  $x$  where the curvature  $\kappa(x)$  of the L-curve  $y(x)$  is maximum. The curvature of a 2D curve expressed as  $y(x)$  is given by  $\kappa(x) = y''(x)/(1 + (y'(x))^2)^{3/2}$ . Since  $y'(x) = 4ax^3 + 3bx^2 + 2cx + d$  and  $y''(x) = 12ax^2 + 6bx + 2c$ , we easily get an analytic expression for the L-curves curvature and its derivative  $\kappa'(x)$ . In practice, we have discrete sampling of these curves and the optimal  $\lambda$  is then simply given by the  $\lambda$  associated with the discrete  $x$  value where  $\kappa'(x) = 0$ . Note that this is an automatic way to find the optimal  $\lambda$ . We show several L-curves in the Results.

### High-Order Anisotropy Measures from ADC Profiles

The ultimate goal when estimating and denoising the diffusivity profile is to use it to infer the underlying diffusion process. This is commonly done using anisotropy measures defined on the set of coefficients used to describe the ADC profile. In the literature, there are two classes of high-order anisotropy measures based on the diffusion profile of HARDI data. One class is defined on the coefficients of a SH series (Frank (15), Alexander et al. (16), Chen et al. (17)) and the other on the independent elements of a HODT (Ozarslan et al. (14)). One important advantage of our algorithm is that we have a handle on both the SH and the HODT coefficients and we thus can implement all these measures.

### Frank and Chen et al. Measures

The two measures found in the Frank (15) and Chen et al. (17) papers are similar and based on SH coefficients. Frank proposed a simple fractional multifiber index (FMI) that is the ratio of the sum of squared high-order coefficients over order-2 coefficients. It is given by

$$FMI = \frac{\sum_{\{j:\ell \geq 4\}} |c_j|^2}{\sum_{\{j:\ell = 2\}} |c_j|^2} \quad [19]$$

Chen et al. (17) claim that the FMI ratio was insufficient to separate isotropic, one-fiber, and multifiber behavior within a voxel. They decided to introduce the variance of the ADC profile about its mean into the characterization of the underlying diffusive behavior with the following ratios:

$$R_0 = \frac{|c_0|}{\sum_j |c_j|}, \quad R_2 = \frac{\sum_{\{j:\ell=2\}} |c_j|}{\sum_j |c_j|}, \quad R_{multi} = \frac{\sum_{\{j:\ell \geq 4\}} |c_j|}{\sum_j |c_j|}, \quad [20]$$

In their paper, they restricted the maximum number of fibers in a voxel to 2 and they used a rank-4 approximation. Hence, they only used  $R_0$  and  $R_2$  ratios. We generalize their approach for more than two directions and use a rank-8 estimation.  $R_{multi}$  is a natural multifiber ratio extension. These anisotropy ratios can be used to formulate a three-step algorithm to distinguish among isotropic, one-fiber, and multifiber diffusion. That is, large  $R_0$  and/or small ADC variance is isotropic; if not, then large  $R_{multi}$  is multifiber; anything else is one-fiber. As mentioned in (39), there are several thresholds involved in this method that must be carefully picked by performing tests on synthetic data to obtain the best results. To overcome the previous limitations, Chen et al. proposed to use cumulative residual entropy (CRE) (40) in their recent paper (39). They used this new information theory measure together with the estimated diffusivities and claimed that it can classify diffusion processes with only two ratios. We choose not to implement it because it is outside the scope of this paper. CRE is based on a probability measure computed from the discrete ADC profile estimates whereas we are focusing on measures defined from the coefficients of the SH or HODT vector parameterizing the ADC profile. A longer discussion can be found in (28).

### Alexander et al. Measure

Alexander et al. used ANOVA (16) to determine whether truncating the series at a higher order as opposed to a lower order significantly changes the fit to the model data. The  $F$  test is

$$F(M_2, M_k) = \frac{(n_s - p_k - 1)(Var(M_k) - Var(M_2))}{(p_k - p_2)E(M_k)}, \quad [21]$$

where  $E$  is the mean squared error between the true ADC profile and the estimated ADC profile at the  $n_s$  sampled points and  $p_k$  is the number of free parameters in model  $M_k$ . In our case, the lower order model is  $M_2$  (order-2 diffusion tensor) and we test it against higher order approximation models  $M_k$ , for  $k = 4, \dots, \ell$ . In (16), ANOVA was used to dynamically choose the order of the SH series approximation.

<sup>2</sup>Before a polynomial curve can be fit, there is a necessary sorting of the  $x$  and the corresponding  $y$  and associated  $\lambda$ . Otherwise, the curve can potentially come back on itself.

### Generalized Anisotropy Measure

Ozarslan et al., in their recent article (12), generalized the well-known DTI FA (fractional anisotropy) measure for HARDI data fitted with high-order tensors. Their generalized anisotropy (GA) measure is based on the generalization of the trace, generalized mean diffusivity, and the variance of the normalized diffusivity of high-order tensors. Due to space restriction, we refer the reader to (12,28) for the complete derivation and a detailed discussion. Contrary to ratios/measures/algorithms proposed from spherical harmonic coefficients reviewed in the previous sections. GA is based the coefficients of the HODT, has the property of being scaled between 0 and 1 and does not assume any specific approximation order.

## METHODS

### Synthetic Data Generation

To evaluate the performance of our fitting procedure, we generate synthetic data using the multitensor model (16,25,28). This model assumes that single fiber responses can be described by a Gaussian (rank-2 tensor) and that the tissue in a voxel with more than one fiber is simply composed of multiple Gaussian fibers that do not exchange molecules. The precise steps to generate the diffusion weighted signal are as follows:

1. Set diffusion encoding gradient directions  $\mathbf{g}_i = (\sin\theta_i, \cos\phi_i, \sin\theta_i \sin\phi_i, \cos\theta_i)^T$  using 3rd-order tessellation of the icosahedron.
2. Set the number of fibers to a specific  $n$  between 0 and 3 (0 is for isotropic signal).
3. For each fiber  $1 \leq k \leq n$ , randomly choose an orientation  $(\theta_k, \phi_k)$  and a relative weight  $p_k$  for the  $k$ th fiber, where  $\sum_{k=1}^n p_k = 1$ . In practice, we impose a minimum angle between fibers of  $45^\circ$  and relative weights between 0.3 and 0.7 for 2-fiber and between 0.2 and 0.4 for 3-fiber distributions. Otherwise, the fiber compartments are too weak to distinguish them.
4. For the isotropic voxels, we use a profile with eigenvalues  $[700, 700, 700] \times 10^{-6} \text{ mm}^2/\text{s}$ . For the other distributions, we generate  $3 \times 3$  tensors with eigenvalues  $[\lambda_1, \lambda_2, \lambda_3] = [200, 200, 1700] \times 10^{-6} \text{ mm}^2/\text{s}$  and generate each fiber tensor  $\mathbf{D}_k$  using rotation matrix  $\mathbf{Rot}$  to orient the main axis of the tensor in direction  $(\theta_k, \phi_k)$ , i.e.,  $\mathbf{D}_k = \mathbf{Rot}^T(\theta_k, \phi_k)\text{diag}(\lambda_1, \lambda_2, \lambda_3)\mathbf{Rot}^T(\theta_k, \phi_k)$ . Note that we choose tensor profiles with anisotropy (RA = 0.72) nearly as high as the most anisotropic regions found in the human brain. This facilitates the discrimination of 2-and 3-fiber distributions. As in (33), the underlying assumption is that lower anisotropy levels are due to noise and partial volume averaging from fibers crossing, kissing, or diverging.
5. Pick a  $b$ -factor and for each encoding direction  $i$  generate the diffusion signal

$$S(\mathbf{g}_i) = S_0 \sum_{k=1}^n p_k e^{-b\mathbf{g}_i^T \mathbf{D}_k \mathbf{g}_i}. \quad [22]$$

6. Add complex Gaussian noise (34) with a standard deviation (std) of  $\sigma = S_0/35$  to the raw signal of Eq. [22]. That is, to each  $S(\mathbf{g}_i)$ , we add a random complex number with independent real and imaginary parts coming from a zero mean Gaussian distributions with  $\sigma = 1/35$  ( $S_0 = 1$ ) and take the modulus to obtain the noisy synthetic data. Recent works (13,16,25) use a similar noise level even though typical real HARDI acquisitions tend to be corrupted by more noise. In our simulations, we need a relatively low noise level in order to characterize 2- and 3-fiber distributions.

This makes computation using this model relatively straightforward. We are trying to obtain the diffusivity profile, however, rather than the signal itself and so, we wish to find  $D(\mathbf{g})$  such that

$$D(\mathbf{g}) = -\frac{1}{b} \ln \left( \frac{S(\mathbf{g})}{S_0} \right) = -\frac{1}{b} \ln \left( \sum_{k=1}^n p_k e^{-b\mathbf{g}^T \mathbf{D}_k \mathbf{g}} \right). \quad [23]$$

The multitensor model has also been used for synthetic data experiments by other authors (e.g., Tuch (22)) and it is worth mentioning that the hindered cylinder model is also another popular synthetic data generation cylinder model used in other works (12,35,36). In this formulation, Soderman and Jonsson (37) assume that fibers are perfect cylinders and that water molecules are confined to diffuse within the walls of these cylinders. In the presence of multiple fibers, the signal attenuation from the cylinders is additive. This gives a more physically based mixture model but is less realistic than the multitensor model that corresponds more closely to empirical fiber data. In any case, the approaches have the same model selection and fitting problems (38).

### Simulations

In order to find the optimal  $\lambda$  for our regularization algorithm, we must plot the L-curves for 1-, 2-, and 3-fiber distributions. It is important to note that there is a different optimal  $\lambda$  depending on the underlying fiber distribution. In fact, in the cases of 1 or no fibers, a high-order tensor formulation is unnecessary and, thus, it is expected to obtain a higher optimal  $\lambda$  for these cases than for multiple fiber diffusion. As previously described under Theory, we need to plot the data errors  $\|\mathbf{X} - \mathbf{BC}\|^2$  on the abscissa and the regularization term  $\mathbf{C}^T \mathbf{LC}$  on the ordinate while incrementally varying  $\lambda \in [0, 0.5]$ . We systematically increment  $\lambda$  by 0.0005 for each set of simulated data. Hence, we simulate three separate tests with 1-, 2-, and 3-fiber distributions, respectively. We decide to choose a relatively high  $b$  value,  $b = 3000 \text{ s/mm}^2$ , to be able to better distinguish 2 and 3 fibers within a voxel as noted in (25). A  $b$  value of  $1000 \text{ s/mm}^2$  is more standard for clinical diffusion MRI acquisitions but research-oriented acquisitions tend use higher  $b$ -factors like the rat biological phantom presented in the next section and data reported in (6,16,22), for example. We perform an order-8 approximation. For each L-curve plot, note that the number of fibers in the simulated diffusion profile, the noise level and the approximation order  $\ell$  are the same for all green points whereas the  $\lambda$  parameter, the relative weights ( $p_k$ 's) of

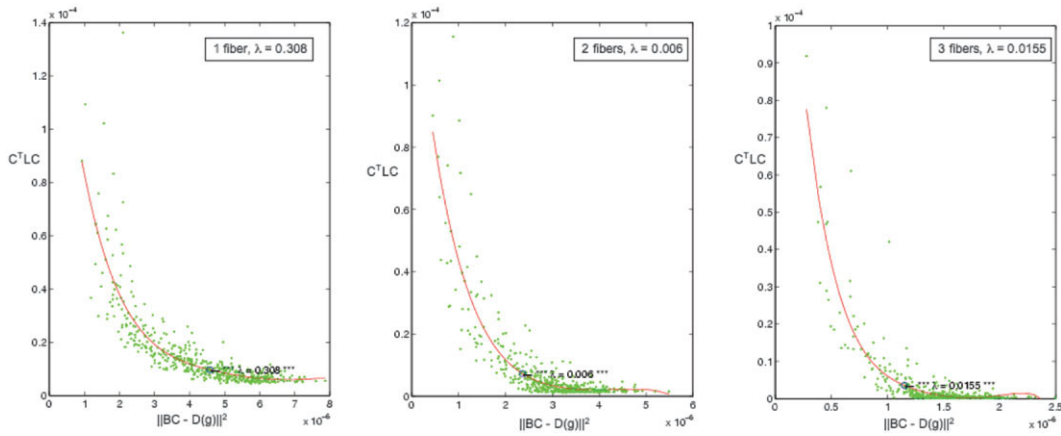


Fig. 5. L-curves for 1, 2, and 3 fibers with optimal  $\lambda$  circled. Points represent data perturbation errors and regularization errors ( $\|\mathbf{X} - \mathbf{BC}\|^2, \mathbf{C}^T\mathbf{LC}$ ).

fibers, and the orientation angle(s) and angle(s) between fibers change for every point in the graph.

One can now ask how valid these optimal  $\lambda$ 's really are and, in particular, how well do they agree with the initial true signal without noise? Hence, in order to verify the L-curve optimal values, we test the effectiveness of recovering the original (without noise) synthetic diffusivity profile from noisy sparse data measurements as above. In doing so, we compare our algorithm with SH estimation without regularization of (15,16) and HODT fitting of (14). For our algorithm,  $\mathbf{T}$  is obtained from Eq. [18]. For Ozarslan et al. (14), we use Eq. [9] to obtain  $\mathbf{T}$  and for the unsmoothed SH technique, we use Eq. [5] to obtain  $\mathbf{C}$ , which is essentially the same as techniques proposed by Frank (15) and Alexander et al. (16) except that their spherical harmonics basis is different. In the latter case, we must apply our transformation matrix  $\mathbf{M}^{-1}$  (Eq. [17]) to obtain  $\mathbf{T}$ . For all cases, we obtain the estimated diffusion profiles on the unit sphere for any angle using Eq. [7]. In

the following, the errors recorded are the mean and standard deviation (std) of the error vector specified by the pointwise absolute difference between points on the estimated ADC and points on the true ADC profiles (Eq. [23] before adding noise) for different regularization parameter  $\lambda$ . We generate a single simulation with 1000 synthetic diffusivity profiles of 1, 2, and 3 fibers mixed together.

Real Data Acquisitions

A Biological Phantom

We also test our regularized estimation algorithm on a biological rat phantom. It was produced by Campbell et al. at the McConnell Brain Imaging Center and Montreal Neurological Institute (6) on a 1.5-T Sonata MR scanner using a knee coil. It was created from two excised Sprague-Dawley rat spinal cords embedded in 2% agar. The acquisition was done with a single-shot spin-echo planar sequence with twice-refocused balanced gradients, designed

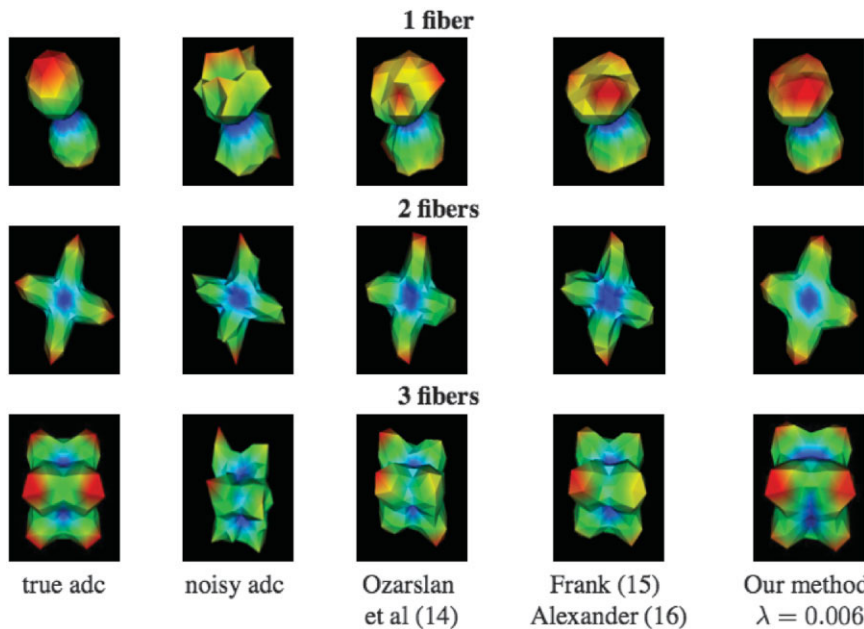


Fig. 6. Visualizing the spherical data fitting procedure for different techniques in the literature. We have in rows 1, 2, and 3 the profiles for a single, for two orthogonal, and for three orthogonal synthetic fibers.

Table 1  
Numerical Simulation to Test the Behavior of Our Algorithm with Varying Regularization Parameter  $\lambda$

|      | LR    | 0     | 0.006 | 1-fiber test with $\lambda$ |       |       |       |
|------|-------|-------|-------|-----------------------------|-------|-------|-------|
|      |       |       |       | 0.012                       | 0.1   | 0.3   | 0.5   |
| Mean | 0.083 | 0.083 | 0.071 | 0.068                       | 0.052 | 0.051 | 0.054 |
| Std  | 0.064 | 0.063 | 0.051 | 0.046                       | 0.036 | 0.035 | 0.037 |
|      | LR    | 0     | 0.003 | 2-fiber test with $\lambda$ |       |       |       |
|      |       |       |       | 0.006                       | 0.009 | 0.012 | 0.015 |
| Mean | 0.076 | 0.075 | 0.070 | 0.069                       | 0.070 | 0.070 | 0.072 |
| Std  | 0.052 | 0.052 | 0.043 | 0.041                       | 0.040 | 0.041 | 0.042 |
|      | LR    | 0     | 0.006 | 3-fiber test with $\lambda$ |       |       |       |
|      |       |       |       | 0.009                       | 0.012 | 0.015 | 0.1   |
| Mean | 0.092 | 0.092 | 0.049 | 0.040                       | 0.034 | 0.031 | 0.057 |
| Std  | 0.037 | 0.037 | 0.028 | 0.026                       | 0.025 | 0.025 | 0.026 |

Note. LR corresponds to the Ozarslan et al. linear regression method (14), Eq. [9]. We report the mean and standard deviation of the pointwise absolute difference between true (without noise) and estimated diffusion profiles.

to reduce eddy current effects. While we use a 3rd-order tessellation of the sphere to obtain our 81 gradient directions on the sphere, they used a high angular resolution dataset acquired with 90 pairs of points (positive and negative) isotropically spaced diffusion encoding directions on the whole sphere generated using electrostatic repulsion algorithm (6). The  $q$ -ball protocol (22) was used with  $b = 3000 \text{ s/mm}^2$ ,  $q = 0.35 \text{ }\mu\text{m}^{-1}$ ,  $\text{TR} = 8 \text{ s}$ ,  $\text{TE} = 110 \text{ ms}$ , 2.8-mm isotropic voxels, 30 slices, and four signal averages per direction.

#### Human Brain Data

Second, we test our method on a real human brain. Diffusion weighted images were acquired at the Center for Magnetic Resonance Research, University of Minnesota, on a 3-T Siemens MagnetomTrio whole-body scanner. We generate 162 gradient directions with a 3rd order tessellation of the icosahedron, as seen in Fig. 2. In practice, assuming symmetry of the diffusion process, we use only one of two directions to obtain 81 gradient directions on the sphere. We acquired three repetitions per direction, each with  $b = 1000 \text{ s/mm}^2$ ,  $\text{TR} = 5100 \text{ s}$ , and  $\text{TE} = 109 \text{ ms}$ . The three measurements are averaged by default by the scanner to produce 81 individual measurements to process. The voxel size was  $3 \text{ mm}^3$  and there were twenty-four  $64 \times 64$  slices.

## RESULTS AND DISCUSSION

### L-Curves and Optimal Regularization Parameter

The L-curves for 1-, 2-, and 3-fiber distributions are plotted in Fig. 5. Each curve was created separately by estimating the diffusion profile while incrementally varying  $\lambda$  by 0.0005 from synthetic noisy diffusion profiles with random fiber orientations and fiber compartments fractions. We show the set of measured points ( $\|\mathbf{X} - \mathbf{BC}\|^2$ ,  $\mathbf{C}^T \mathbf{LC}$ ), the fitted L-curve, and indicate the optimal estimated  $\lambda$  with a circle.

From the L-curves and the automatic procedure described under Theory, *Finding Optimal Regularization Parameter with the L-Curve Method*, the optimal  $\lambda$  are 0.308,

0.006, and 0.0155 for 1-, 2-, and 3-fiber distributions, respectively.

In order to verify these optimal L-curve  $\lambda$  values, we tabulate the mean and standard deviation (std) of the pointwise absolute difference between the true and estimated ADC profiles of the 1000 synthetic diffusion profiles generated with 1, 2, and 3 fibers, as described under Method. From Table 1, there are several expected observations that one can make. First, from the first two columns, we note that the LR fit of a HODT (Eq. [9]) and the SH series fit with no regularization (Eq. [5]) are the same up to a very small numerical error. As previously discussed, this is to be expected because the two models are equivalent and there exists a direct change-of-basis transformation between the two (Eq. [17]). Second, as observed with the L-curve, single fiber voxels are optimally fit with larger  $\lambda$  than in the multiple fiber voxels. This occurs because in the case of a single fiber, higher-order estimation is unnecessary. Intuitively, a large  $\lambda$  in Eq. [15] cancels the effect of high-order tensor terms so that the model is closer to a rank-2 tensor formulation. However, as soon as we have more structure, as in the cases of 2 or 3 fibers,  $\lambda$  of 0.006 and 0.015 are best, respectively. This is expected as we need to maintain significant contributions from higher-order terms in order to accurately fit multifiber ADC profiles. If this is so, one can wonder why the optimal  $\lambda$  for 3 fibers is higher than for 2-fiber distributions. This is because as fibers are added within a voxel, the signal tends to be more isotropic due to partial volume averaging. Thus, the need for higher terms becomes less needed in the approximation. It is important to note that these best simulated  $\lambda$  values closely agree with the L-curve points of maximum curvature, which validates the automatic and analytic L-curve optimal  $\lambda$  procedure. Finally, note that the optimal value in the 2-fiber case is quite broad for different  $\lambda$  values, which suggests that there is a range of possible  $\lambda$  one can choose without changing the resulting estimation. In practice, we have noted that the exact optimal  $\lambda$  chosen is flexible within a small range that depends on the dynamics of the signal. Nonetheless, since in all cases  $\lambda = 0.006$  performs better than both LR and the SH fit with  $\lambda = 0$  and the optimal value found with the L-curve

Table 2  
Mean GA Measure over 10000 Simulated ADC Profiles

|           | Our method ( $\lambda = 0.006$ ), LR |            |            |                           |
|-----------|--------------------------------------|------------|------------|---------------------------|
|           | $\ell = 2$                           | $\ell = 4$ | $\ell = 6$ | $\ell = 8$                |
| 1 fiber   | 0.92, 0.92                           | 0.92, 0.92 | 0.92, 0.92 | 0.92, 0.92                |
| 2 fibers  | 0.64, 0.65                           | 0.71, 0.73 | 0.72, 0.73 | 0.70, 0.71                |
| 3 fibers  | 0.09, 0.09                           | 0.19, 0.21 | 0.20, 0.13 | 0.10, 0.09                |
| Isotropic | 0.09, 0.09                           | 0.09, 0.10 | 0.09, 0.09 | $8 \times 10^{-4}$ , 0.01 |

Note. Mean GA calculated from our algorithm and Ozarslan's LR method. We observe similar overall behaviors to the ones reported in (12, Table 4).

in the case of 2 fibers is  $\lambda = 0.006$ , we choose to set  $\lambda = 0.006$  for the rest of the paper. This avoids having to compute optimal  $\lambda$  at each voxel of the dataset.

Qualitatively, Fig. 6 illustrates how we obtain a smoother ADC profile estimation that visually agrees with our quantitative results. Our regularized tensor estimation gives a diffusivity profile closer to the true ADC without noise. Here, we have stretched the surface mesh with respect to each ADC profile value  $D(\mathbf{g}(\theta_i, \phi_i))$ . The color map is red for high values and blue for low ADC values.

### High-Order Anisotropy Measures Results

We implemented the high-order anisotropy measures defined under Theory, *High-Order Anisotropy Measures from ADC Profiles*, to study their ability to identify the underlying synthetic diffusion process. We have used the same synthetic data generation process as before with Gaussian complex noise with standard deviation  $\sigma = 1/35$  and  $b = 3000$  s/mm<sup>2</sup>. We create a large set of simulated profiles where the number of fibers is picked randomly between 0 and 3. Our goal is to correctly classify synthetic noisy data, generated as before, into three classes: isotropic diffusion, 1-fiber anisotropic diffusion, and multifiber diffusion, i.e., diffusion corresponding to either 2 or more fibers.

First, we show the results of computed GA values in Table 2 for different order approximations. Even though the exact values are different because we use a different synthetic data generation, we are able to reproduce the same behaviors of the GA measure published by Ozarslan et al. (12, Table 4). In particular, for a single fiber, the measures are almost independent of the rank being used for the estimation (first row in Table 4 (12)). However, GA measures are significantly higher for rank-{4,6,8} than for the rank-2 model when there are multiple fibers. There is

also an overlap in GA values between diffusion in 3-fiber distributions and isotropic diffusion. It is in these cases that the rank-2 model is unsatisfying.

We have computed a similar table for all other anisotropy measures (not shown here). One can then attempt to find the best thresholds that separate the different measures into these three classes for all anisotropy measures. We test the robustness of the classifications with and without smoothing parameter while changing the rank of the approximation. We also analyze the behavior of the different measures by recording the classification success rate.

From Table 3, we see that the best results for Chen et al. (Eq. [20]) and ANOVA (Eq. [21]) obtained from  $\lambda = 0.006$  produce better classification percentages than the best outcome of FMI (Eq. [19]). FMI is the simplest of the measures and is not able to capture as many details as the other two methods, which include statistical information and a better comparison between estimation order used to model the data. The advantage of the Chen et al. algorithm over other measures is that it involves well-chosen SH coefficient ratios and the variance of ADC profile about its mean. Experimentally, we find it more robust to noise and less sensitive to the threshold selection. In fact, we do not have to adapt thresholds between tests when changing  $\lambda$  and the rank of the HODT. This is not the case with ANOVA.

It is also important to note the better performance of our regularization procedure with a nonzero  $\lambda$  used in conjunction with the Chen et al. and the ANOVA measures than with no regularization ( $\lambda = 0$ ). This illustrates the added value brought by our regularization method. This is because the estimated ADC profile is smoother, and hence, the SH and HODT coefficients incorporate less noise. On the other hand, for FMI measure, we note that it performs better when  $\lambda = 0$ . This is not surprising because of the nature of the ratio and, in particular, because the numerator depends only on high-order terms of the SH series. With a nonzero  $\lambda$ , the coefficients of higher order are penalized and therefore have lower values than without a smoothing term. The ratio is thus not designed to be used with our method. Note also the higher success rate of the GA measure compared with the other measures. Being a high-order generalization of FA, it is better theoretically founded and its characterization is better than with "ad hoc" ratios on SH coefficients. In our experiments, we also note that the GA values are more stable, i.e., have fewer variations between random trials, which makes it easier to find the best thresholds.

Table 3  
Success Rate for the Classification of Synthetic Voxels into Isotropic, 1-Fiber, and Multifiber Diffusion Class Using Different High-Order Anisotropy Measures

|            | FMI (Eq. [19]) |                   | Chen (Eq. [20]) |                   | ANOVA (Eq. [21]) |                   | GA            |                   |
|------------|----------------|-------------------|-----------------|-------------------|------------------|-------------------|---------------|-------------------|
|            | $\lambda = 0$  | $\lambda = 0.006$ | $\lambda = 0$   | $\lambda = 0.006$ | $\lambda = 0$    | $\lambda = 0.006$ | $\lambda = 0$ | $\lambda = 0.006$ |
| $\ell = 8$ | 93.1%          | 85.1%             | 83.2%           | 96.0%             | 91.7%            | 94.8%             | 99.9%         | 99.8%             |
| $\ell = 6$ | 93.1%          | 84.2%             | 89.1%           | 97.0%             | 90.9%            | 94.5%             | 99.6%         | 99.8%             |
| $\ell = 4$ | 83.2%          | 82.2%             | 93.1%           | 97.0%             | 88.7%            | 91.1%             | 99.9%         | 100%              |
| $\ell = 2$ |                |                   | 54.4%           | 54.5%             |                  |                   | 97.6%         | 97.6%             |

Note. For each measure, we select thresholds that best distinguish the three class. FMI and ANOVA measure make no sense in the  $\ell = 2$  case.

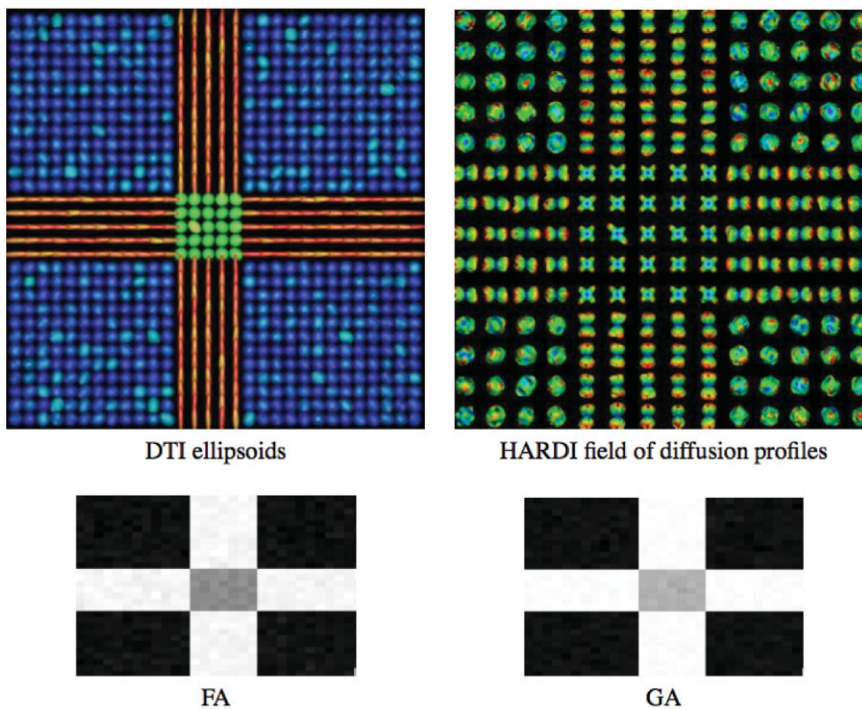


Fig. 7. Two orthogonal fiber bundles crossing at  $90^\circ$ . The color map for the DTI ellipsoids is blue for isotropic, green for planar, and red for anisotropic ellipsoids. Note that ellipsoids are flat and have no preferred principal direction in the crossing area whereas ADC profiles have multiple peaks. [Color figure can be viewed in the online issue, which is available at [www.interscience.wiley.com](http://www.interscience.wiley.com).]

In order to validate the approach on a field of noisy spherical functions, we have also extended our single voxel synthetic generation to construct a noisy high angular resolution  $30 \times 30$  slice with a  $5 \times 5$  crossing configuration in the center of Figs. 7 and 8. The ADCs were estimated with an order 6 spherical harmonic series and  $\lambda = 0.006$ .

We perform one experiment with two and another with three orthogonal fibers crossing. Note that all voxels in this slice have the same mean diffusivity. We compare the shape of the DTI ellipsoids with the shape of the ADC profiles and the resulting FA and GA anisotropy measures. Although we choose only to show results of the FA measure, it is important to note that RA and FA have similar properties (12) and there is no notable differences between the two measures when comparing them against GA. The DTI ellipsoids were computed using standard least-squares fit from all discrete high angular measures. The color map is blue for isotropic, green for planar, and red for anisotropic ellipsoids. While the ellipsoids are flat and have no preferred principal direction in the crossing area of Figs. 7 and 8, the ADC profiles clearly have multiple peaks reflecting multiple fibers. Although the multiple peaks do not agree with the underlying fiber orientations,<sup>3</sup> the high-order anisotropy measures like GA are able to pick up these differences. The limitation of FA measure is even more evident on the 3-fiber distribution example in Fig. 8. The FA measure is in the same range as the background whereas the GA map is able to distinguish the multifiber diffusion processes. In the last row of Fig. 8, we see the effects of varying the threshold separating isotropic

from multifiber diffusion. The thresholds are selected experimentally and we see that the critical threshold is in the range of the mean GA measure of the  $\ell = 8$  column in Table 2. We see that GA values can discriminate among the different diffusion processes with some errors made when there are overlap between noisy 3-fiber distributions and noisy isotropic diffusion signals. If the 3-fiber threshold is too high, some multifiber voxels are incorrectly classified as isotropic and vice versa when the 3-fiber threshold is too low. This is due to noise and partial volume averaging.

Finally, it is worth mentioning that the choice of noise level and  $b$ -factor surely affect the classification results as one would expect. Noisy data makes classification harder for all classes since major overlap appear among 1-fiber, multi and isotropic distributions. A lower  $b$ -value also produces less reliable results in multifiber voxels.<sup>4</sup> This is because the diffusion profiles are wider and less sharp than for a high  $b$ -value.

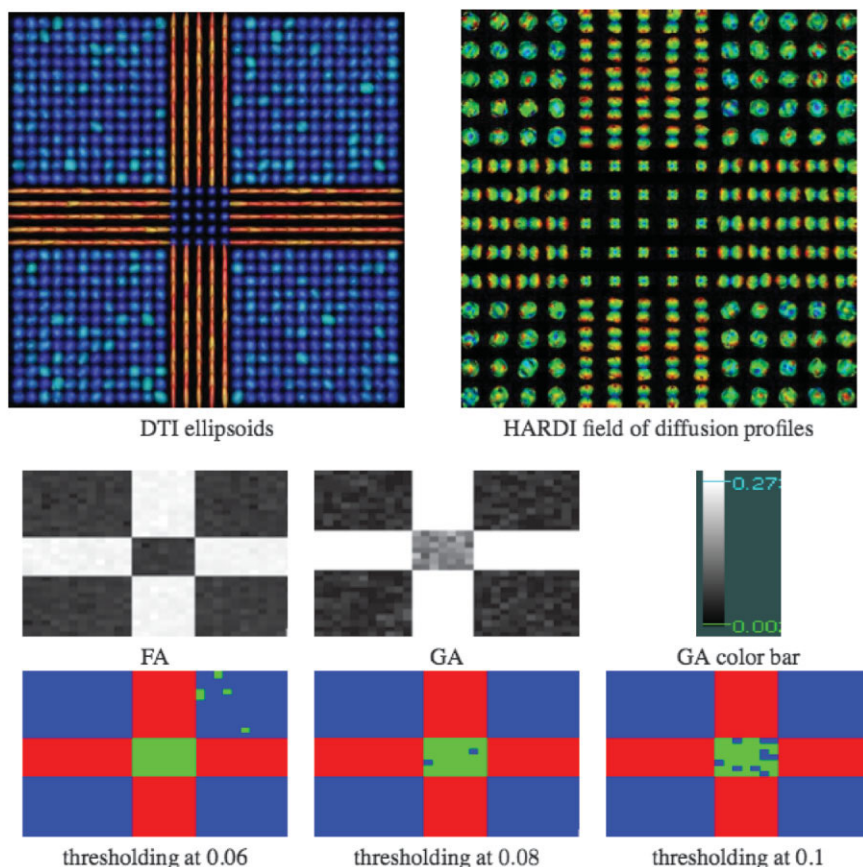
#### A Biological Phantom

Figure 9 shows the results on the rat spinal chords. The baseline  $T_1$ -weighted image illustrating the ground truth configurations of the fibers is seen in the top left of Fig. 9. We compare the ellipsoid surfaces obtained from the standard DTI least-squares fit using all 90 directions against the ADC profile computed with our regularized spherical harmonic estimation. The ellipsoids and ADC profiles are overlaid on the computed GA map. A rank-8 estimation with  $\lambda = 0.006$  was used. As expected, the DTI ellipsoids are planar and tend to be spherical in the crossing area whereas our high-order estimation of the ADC profile re-

<sup>3</sup>Diffusion profile maxima do not agree with fiber directions for two or more underlying fibers. One must define functions in real space like the orientation distribution function (ODF) to extract fiber orientations (see (24)).

<sup>4</sup>This is explicitly illustrated in (24,25,33) in fiber orientation estimation experiments.

Fig. 8. Three orthogonal fiber bundles crossing at 90° where one bundle is coming out of the page. GA can distinguish the crossing area whereas the FA cannot. The last row illustrates the effect of varying the threshold in the classification process. blue, isotropic; red, 1 fiber; green, multifiber class, respectively. Some voxels are incorrectly classified due to noise and partial volume averaging.



covers multiple peaks. Moreover, even though the GA map has slightly noisy background, it recovers both fiber bundles and the measure is different in the crossing than in certain straight single fiber parts. However, contrary to the synthetic data characterization, the GA difference between 1- and 2-fiber regions is not clear enough to fully distinguish the two with simple thresholding.

### Human Brain HARDI Data

Based on expert knowledge of the anatomy and the FA anisotropy measures, we have manually selected voxels

with one and two fibers in the corpus callosum and the corticospinal tract to illustrate the performance of our regularization algorithm on real data. A rank-8 approximation with  $\lambda = 0.006$  was used. Figure 10 shows some of the results.

Classification on real data is a much more difficult task than the synthetic data experiments where the noisy generated signal is more homogeneous and GA statistics are easily computed. On real data, one must manually select regions with known crossings and regions with single fiber anisotropy to analyze the corresponding GA measure be-

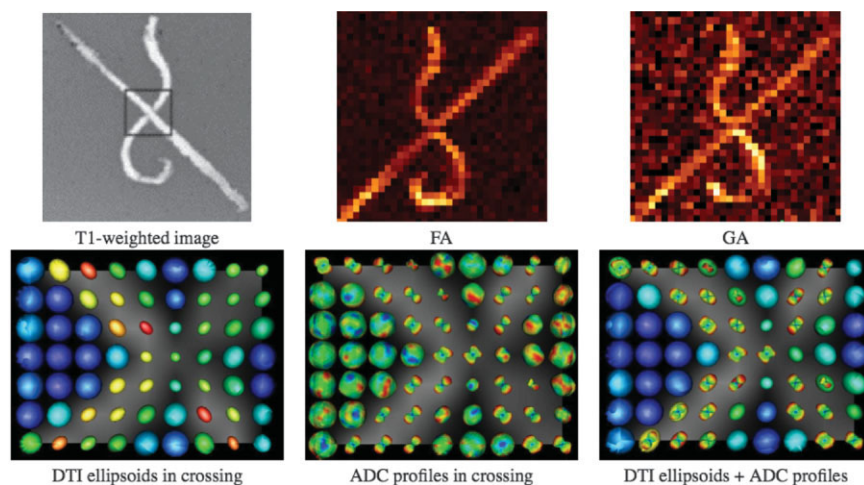


Fig. 9. Biological phantom produced by Campbell et al. (6). We show the baseline  $T_1$ -weighted image and fields of DTI ellipsoids and estimated ADC profiles overlaid on the GA map in the crossing area. The DTI ellipsoids tend to be flat (greenish) and spherical (bluish), whereas the ADC profiles clearly have multiple peaks.

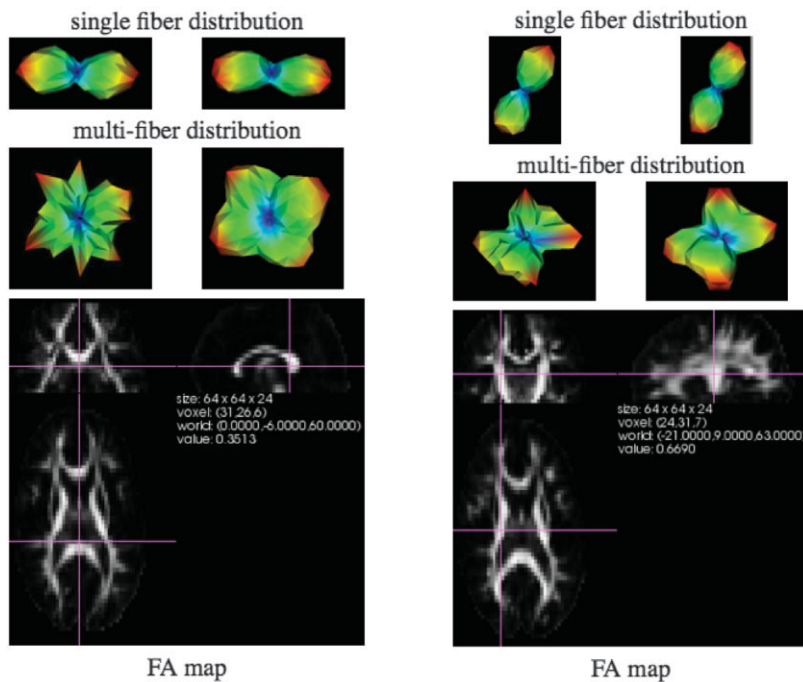


Fig. 10. ADC profiles selected from real data voxels in the corpus callosum and the corticospinal tract. We have manually selected voxels with one and two fibers-based on knowledge of the anatomy and FA measure. The left column in each subfigure represents the real profile and the right column is the estimated ADC profile from our algorithm.

havior. Due to noise and partial volume effects there is too much overlap between diffusion process classes. Nonetheless, we observe that the real data ADC profiles have very similar shapes and properties compared to our synthetic data. Even though we do not believe that one can simply threshold the real data GA map to classify the diffusion process, one can make better use of the GA than FA scalar measure to look for multiple fibers crossing. Visual inspection of the peaks of the ADC profile in the small regions of interest shows agreement with neuroanatomy knowledge (Fig. 10) of single and multiple fiber bundles. In the left subfigure, two profiles were chosen in the corpus callosum, one with 1-fiber and the other with 2-fiber distribution evidence. The FA map illustrates the location where the 2-fiber distribution was extracted with a low FA value of 0.35. In the right subfigure, profiles were extracted from a 1-fiber region of the corticospinal tract and a nearby 2-fiber crossing with the corpus callosum. The FA map shows the location of the 1-fiber diffusion voxel with a high FA value of 0.67.

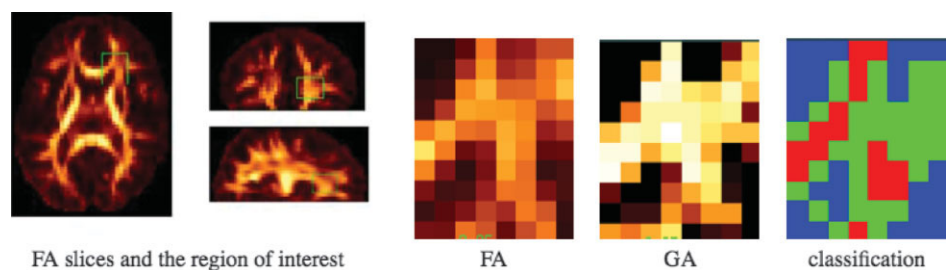
Finally, we reproduce a similar figure as Tuch's in (22, Fig. 12f) from the genu of the corpus callosum in Fig. 11. This region is known to have multiple fibers crossing. We thus observe a lower FA than that found in strong anisotropic areas and a stronger GA value in the range corre-

sponding to 2 or 3 fibers in Table 2. If one locally thresholds this region of interest, the obtained classification provides some valuable information. The multifiber regions in red clearly stand out and we can thus identify areas of transition between single (blue) and multiple (red) fiber diffusion class. The classification of Fig. 11 agrees with voxels containing multiple fiber crossings such as presented in (22, Fig. 12f).

## CONCLUSIONS

Overall, there are several contributions in this paper. First, we proposed a new regularization algorithm to estimate a smoother ADC profile closer to the true ADC profile without noise. We chose a meaningful modified spherical harmonic basis to capture the physical constraints of the problem, defined a regularization term based on the smoothing properties of the Laplace–Beltrami operator for functions defined on the unit sphere, and derived the linear transformation taking SH coefficients to HODT coefficients. We thus obtained a high-order diffusion tensor. The method was tested against state-of-the-art techniques from the literature on synthetic data, on a biological phantom, and on real human brain data. Our experiments verify the equivalence of the diffusion tensor and the spherical

Fig. 11. Region of interest from the genu of the corpus callosum, similar as in Tuch (22, Fig. 12f). We show FA, GA, and the thresholded classification map obtained. Green, multi-fiber; red, 1 fiber; blue, isotropic diffusion class, respectively. Green voxels agree with known crossings in that area.



harmonic formulations of the diffusivity profile up to a good numerical approximation. This is useful because it implies that any technique developed for the spherical harmonic formulation can be quickly and easily applied to the diffusion tensor formulation and vice versa.

Moreover, the continuous smoothing parameter  $\lambda$  generalizing the traditional least-squares fitting algorithm for spherical harmonic series is appropriate whenever there is a sparsely sampled set of noisy data on a sphere and the expected approximation function is relatively smooth. However, minimizing the squared error is not the only important characteristic of a good approximation function. In particular, if we wish to be able to extract a fiber probability distribution for the voxel from our diffusivity profile model, we need the approximation to be sufficient to capture details up to the desired level of resolution. For example, over a data set that contained a large proportion of voxels with only a single fiber direction, an order-2 fit would certainly minimize the squared error from the actual data averaged over the entire data set. However, the higher-order voxels would be modeled very poorly, making various tasks, such as tractography, considerably more difficult. For this reason, simple truncation, which is the equivalent to fitting the data with a lower-order tensor is not comparable to a procedure that retains higher-order detail, such as the proposed fit with a well-chosen regularization weight  $\lambda$ . Up to the resolution that we were considering, order-4 truncation was a valid choice of fitting procedure but has neither the general applicability nor the ability to retain detail at the 6th and 8th orders shown by the smoothness maximizing criterion we propose.

In addition to these contributions, another important part of the paper is the careful study of the existing anisotropy measures for SH and HODT parameterization of the HARDI ADC profiles. We extended the study by attempting to classify the diffusion process from these anisotropy measures. This proved to be easier on synthetic data than on real data, where selecting sensible thresholds is much harder. We have successfully reproduced the properties of the GA measure and clearly showed its advantages over the other scalar indices computed from spherical harmonics coefficients. In addition to being the high-order generalization of the popular FA measure for DTI, it is stable and has the advantage of being scaled between 0 and 1. With a fast visual inspection, this allows the detection of non-Gaussian diffusion processes in cerebral regions from real data. This can potentially be of great help to clinicians and neurosurgeons.

## ACKNOWLEDGMENTS

We thank the Editor and reviewers for making very constructive comments that have considerably strengthen the paper. The authors thank the McConnell Brain Imaging Center of McGill University and especially J.S.W. Campbell, P. Savadjiev, K. Siddiqi, V. V. Rymar, and B. G. Pike for the rat cord dataset. This exchange was supported by the FFCR grant, the CRSNG Canada graduate scholarship and INRIA International internships program. Moreover, thanks to S. Lehericy and K. Ugurbil at the Center for Magnetic Resonance Research at the University of Minne-

sota for the high angular human brain dataset. Thanks also to G. Sapiro from the ECE, University of Minnesota. This part was partially supported by grants NSF-INRIA Cooperative Research. The authors would like to thank M. de La Gorce and C. Lenglet for useful discussion and valuable inputs.

## REFERENCES

1. LeBihan D, Breton E, Lallemand D, Grenier P, Cabanis E, Laval-Jeantet M. MR imaging of intravoxel incoherent motions: application to diffusion and perfusion in neurologic disorders. *Radiology* 1986;161:401–407.
2. Basser PJ, Mattiello J, LeBihan D. Estimation of the effective self-diffusion tensor from NMR spin echo. *J Magn Reson B* 1994;123:247–254.
3. Tschumperlé D, Deriche R. Variational frameworks for DT-MRI estimation, regularization and visualization. In: *Proceedings of the 9th International Conference on Computer Vision, Nice, France, 2003*. p. 116–121.
4. Wang Z, Vemuri BC, Chen Y, Mareci T. Simultaneous smoothing and estimation of the tensor field from diffusion tensor MRI. In: *Proceedings of the IEEE Conference on Computer Vision and Pattern Recognition*, volume 1. Madison, WIS, USA, 2003. p. 461–466.
5. Westin C-F, Maier SE, Mamata H, Nabavi A, Jolesz FA, Kikinis R. Processing and visualization of diffusion tensor MRI. *Med Image Anal* 2002;6:93–108.
6. Campbell JSW, Siddiqi K, Rymar VV, Sadikot A, Pike BG. Flow-based fiber tracking with diffusion tensor  $q$ -ball data: validation and comparison to principal diffusion direction techniques. *NeuroImage* 2005;27:725–736.
7. Lenglet C, Rousson M, Deriche R, Faugeras O. Statistics on the manifold of multivariate normal distributions: theory and application to diffusion tensor MRI processing. *J Math Imaging Vis, Special Issue MIA 2006*, (in press). (Available at <ftp://ftp-sop.inria.fr/odyssey/Publications/2005/lenglet-rousson-etal:05b.pdf>).
8. Lenglet C, Rousson M, Deriche R, Faugeras O, Lehericy S, Ugurbil K. A Riemannian approach to diffusion tensor images segmentation. In: *Proceedings of the 19th International Conference on Information Processing in Medical Imaging (IPMI)*, Glenwood Springs, CO, USA, 2005. p. 591–602.
9. Poupon C. Détection des faisceaux de fibres de la substance blanche pour l'étude de la connectivité anatomique cérébrale. Ph.D. thesis, Ecole Nationale Supérieure des Télécommunications, 1999.
10. Doug Q, Welsh RC, Chenevert TL, Carlos RC, Maly-Sundgren P, Gomez-Hassan DM, Mukherji SK. Clinical applications of diffusion tensor imaging. *J Magn Reson Imaging* 2004;19:6–18.
11. Basser PJ, Pierpaoli C. Microstructural and physiological features of tissues elucidated by quantitative diffusion tensor MRI. *J Magn Reson B* 1996;111:209–219.
12. Ozarslan E, Vemuri BC, Mareci T. Generalized scalar measures for diffusion MRI using trace, variance and entropy. *Magn Reson Med* 2005;53:866–876.
13. Tuch DS. Diffusion MRI of complex tissue structure. Ph.D. thesis, Harvard University and Massachusetts Institute of Technology, 2002.
14. Ozarslan E, Mareci T. Generalized diffusion tensor imaging and analytical relationships between diffusion tensor imaging and high angular resolution imaging. *Magn Reson Med* 2003;50:955–965.
15. Frank LR. Characterization of anisotropy in high angular resolution diffusion-weighted MRI. *Magn Reson Med* 2002;47:1083–1099.
16. Alexander DC, Barker GJ, Arridge SR. Detection and modeling of non-Gaussian apparent diffusion coefficient profiles in human brain data. *Magn Reson Med* 2002;48:331–340.
17. Chen Y, Guo W, Zeng Q, Yan X, Huang F, Zhang H, He G, Vemuri BC, Liu Y. Estimation, smoothing, and characterization of apparent diffusion coefficient profiles from high angular resolution DWI. In: *Proceedings of the IEEE Conference on Computer Vision and Pattern Recognition*, volume 1, Washington, DC, USA, 2004. p. 588–593.
18. Stejskal EO, Tanner JE. Spin diffusion measurements: spin echoes in the presence of a time-dependent field gradient. *J Chem Phys* 1965;42:288–292.

19. Savadjiev P, Campbell JSW, Pike BG, Siddiqi K. 3D curve inference for diffusion MRI regularization. In: Proceedings of the 8th International Conference on Medical Image Computing and Computer-Assisted Intervention (MICCAI). Part 1, LNCS 3749, Palm Springs, CA, USA, 2005. p. 123–130.
20. Tuch DS, Reese TG, Wiegell MR, Makris NG, Belliveau JW, Wedeen VJ. High angular resolution diffusion imaging reveals intravoxel white matter fiber heterogeneity. *Magn Reson Med* 2002;48:577–582.
21. Wedeen VJ, Reese TG, Tuch DS, Dou J-G, Weiskoff RM, Chessler D. Mapping fiber orientation spectra in cerebral white matter with fourier-transform diffusion MRI. In: Proceedings of the 7th Annual Meeting of ISMRM, Philadelphia, PA, USA, 1999. p. 321.
22. Tuch DS. *Q*-ball imaging. *Magn Reson Med* 2004;52:1358–1372.
23. Jansons KM, Alexander DC. Persistent angular structure: new insights from diffusion magnetic resonance imaging data. *Inverse Problems* 2003;19:1031–1046.
24. Descoteaux M, Angelino E, Fitzgibbons S, Deriche R. A linear and regularized ODF estimation algorithm to recover multiple fibers in *q*-ball imaging. Research Report 5768, INRIA, Nov. 2005.
25. Alexander DC, Barker GJ. Optimal imaging parameters for fiber-orientation estimation in diffusion MRI. *NeuroImage* 2005;27:357–367.
26. Gia QTL. Approximation of linear partial differential equations on spheres. Ph.D. thesis, Texas A&M University, 2003.
27. Sochen N, Deriche R, Lopez-Perez L. Variational Beltrami flows over manifolds. In: Proceedings of the IEEE International Conference on Image Processing, volume 1, Barcelona, Spain, 2003. p. 861–864.
28. Descoteaux M, Angelino E, Fitzgibbons S, Deriche R. Apparent diffusion coefficients from high angular resolution diffusion imaging: estimation and applications. Research Report 5681, INRIA, Sept. 2005.
29. Brechbuhler CH, Gerig G, Kubler O. Parameterization of closed surfaces for 3D shape description. *Comput Vis Image Underst* 1995;61:154–170.
30. Hansen PC. The L-curve and its use in the numerical treatment of inverse problems. In: Johnston P, editor. Computational inverse problems in electrocardiology. Southampton:WIT Press; 2001. p. 119–142.
31. Tschumperlé D, Deriche R. Diffusion tensor regularization with constraints preservation. In: Proceedings of IEEE Conference on Computer Vision and Pattern Recognition, Kauai, HI, USA, 2001. p. 948–953.
32. Chefd'hotel C, Tschumperlé D, Deriche R, Faugeras O. Regularizing flows for constrained matrix-valued images. *J Math Imaging Vis* 2004;20:147–162.
33. Tournier J-D, Calamante F, Gadian DG, Connelly A. Direct estimation of the fiber orientation density function from diffusion-weighted MRI data using spherical deconvolution *NeuroImage* 2004;23:1176–1185.
34. Sijbers J, den Dekker AJ, van Audekerke J, Verhoye M, van Dyck D. Estimation of the noise in magnitude MR images. *Magn Reson Imaging* 1998;16:87–90.
35. von dem Hagen EA, Henkelman RM. Orientational diffusion reflects fiber structure within a voxel. *Magn Reson Med* 2002;48:454–459.
36. Ozarslan E, Vemuri BC, Mareci T. Fiber orientation mapping using generalized diffusion tensor imaging. In: IEEE International Symposium on Biomedical Imaging (ISBI), Arlington, VA, USA, April 2004. p. 1036–1038.
37. Soderman O, Jonsson B. Restricted diffusion in cylindrical geometry. *J Magn Reson A* 1995;117:94–97.
38. Alexander DC. An introduction to diffusion MRI: the diffusion tensor and beyond. In: Weickert J, Hagen H, editors. Visualization and image processing of tensor fields. Springer, 2006.
39. Chen Y, Guo W, Zeng Q, Yan X, Rao M, Liu Y. Apparent diffusion coefficient approximation and diffusion anisotropy characterization in DWI. In: Proceedings of the 19th International Conference on Information Processing in Medical Imaging (IPMI), Glenwood Springs, CO, USA, 2005. p. 246–257.
40. Rao M, Chen Y, Vemuri BC, Wang F. Cumulative residual entropy: a new measure of information. *IEEE Trans Inform Theory* 2004;50:1220–1228.